Tellus (1995), 47A, 722–732

TELLUS
ISSN 0280–6495

Numerical simulations of the life cycle of a baroclinic wave

By WILLIAM T. THOMPSON, *Naval Research Laboratory, Marine Meteorology Division, 7 Grace Hopper Ave., Monterey, California 93943-5502, USA*

(Manuscript received 5 September 1994; in final form 3 February 1995)

ABSTRACT

A new conceptual visualization of cyclone-frontal evolution is presented by Shapiro and Keyser (1990). The primary differences between this model and the classical Norwegian frontal cyclone model are the absence of an occlusion, the presence of a warm-core seclusion, and the "bent back" warm front or westward extension of the warm front. In the present study, a mesoscale numerical model is used to investigate the kinematics and structural features of the bent back warm front. Simulations are performed using a 2nd-order closure turbulence parameterization with a sophisticated surface layer similarity scheme. The adiabatic and inviscid case is also examined. Results show that the seclusion and bent back warm front are present in both the adiabatic and inviscid case and using the 2nd-order closure parameterization. An occlusion also forms in later stages in both cases, indicating that the absence of an occlusion in the original publication of the Shapiro and Keyser model is a shortcoming. The results also show that, while the adiabatic components of the flow are responsible for creating the important features of cyclogenesis and frontogenesis, diabatic physical processes exert a strong influence on the ultimate cyclone/frontal structure. Sensitivity studies are performed in order to further investigate this issue.

1. Introduction

In a recent paper, Shapiro and Keyser (1990) (hereinafter SK) present a "conceptual visualization of cyclone-frontal evolution" which represents a major alteration to the Norwegian frontal cyclone model. This alteration to the classical model incorporates many of the features depicted in recent observational and numerical investigations of the life cycles of baroclinic waves and fronts. The fundamental differences between the SK model and the Norwegian model are the absence of an occlusion, the "bent back" warm front or westward extension of the warm front (WEWF), and the presence of a seclusion. The Norwegian model is familiar to the scientific community and the SK model is presented in Fig. 10.27 of SK. Both the absence of an occlusion and the WEWF are attributable to the "frontal fracture" which occurs in the early phase of the amplification of the temperature wave. Frontal fracture occurs when the warm and cold fronts separate near the center of the low.

In the present study, a mesoscale numerical model will be used to investigate the kinematics and structural features of the WEWF in two different idealized simulations. The first of these is an adiabatic and inviscid simulation while the second uses a second-order closure turbulence parameterization and a sophisticated surface layer similarity scheme. Shapiro and Keyser claim that the adiabatic components of the flow are responsible for creating the essential features of cyclogenesis. The adiabatic and inviscid simulation will demonstrate that this is the case. The second-order closure simulation, which provides a more realistic treatment of boundary layer physical processes, will show the impact of these processes on formation of the WEWF and seclusion. Each of the simulations is 120 h (5 days) in length and each uses the same highly baroclinically unstable initial state. Although the results of the two simulations are, not surprisingly, very different, all of the structural features noted above (frontal fracture, WEWF, seclusion, and occlusion) are present in both simulations.

The warm front, cold front, and occluded front have been recognized since the inception of the polar front theory. The structural features and kinematics of these fronts are well understood. The bent-back warm front, however, is not as well documented. The present study constitutes an attempt to gain some understanding of the bent-back warm front or WEWF. Use of the second-order closure parameterization allows investigation of the impact of boundary layer physical processes on structural features of the SK model as well.

2. Model description

The mesoscale model we use is a version of the Navy Operational Regional Atmospheric Prediction System (NORAPS) which is described by Hodur (1987). It is a hydrostatic primitive equation model with a split explicit time integration scheme. The horizontal resolution is 40 km and a sigma coordinate is used in the vertical. In the simulations described herein, 21 vertical levels are used.

In the second-order closure physics, the predictive equations are solved using implicit, tridiagonal finite difference algorithms with upper and lower boundary conditions inserted into the resulting matrices. A form of Gaussian elimination is used to achieve solution. We solve prognostic equations for the U and V components, liquid-water potential temperature, turbulent kinetic energy, and temperature variance. The remaining second-moment turbulence expressions are solved by diagnostic (algebraic) equations. This system of equations is termed a level 3 model in the Mellor and Yamada (1974) classification system.

The model physics includes a Blackadar-type expression for length scale, which is proportional to height near the surface and approaches a limiting value aloft dependent upon moments of the vertical turbulent kinetic energy distribution and a surface layer similarity scheme based of the formulation of Liu et al. (1979). Roughness lengths for momentum and temperature are evaluated in this scheme using an iterative method.

Additional details concerning the model design and model physics can be found in Burk and Thompson (1989).

3. Initial and boundary conditions

The initial conditions for the numerical experiments to be performed consist of a strongly baroclinically unstable regime. This regime involves a $40\ \mathrm{m\ s^{-1}}$ westerly jet at 200 mb at the center of the domain, decreasing to zero at the north and south boundaries with a $\sin^2$ profile. In the vertical, the u component of the wind decreases (linearly in z) to zero at the surface. The jet, which is invariant in the zonal direction, is in geostrophic and thermal wind balance. This implies a strong meridional temperature gradient at all levels with a concentrated baroclinic zone near the center of the grid. The v component consists of an altitude independent 3000 km sinusoidal perturbation in both x and y with a maximum amplitude of $1\ \mathrm{m\ s^{-1}}$ at the center of the domain. The wavelength of the perturbation was chosen to be near the wavelength of maximum instability from linear theory (~ 3250 km). The vertical temperature profile was chosen so as to yield a value of the stability parameter which enhances the growth rate of a 3000 km baroclinically unstable wave. The temperature and pressure gradients and both velocity components are zero at the north and south boundaries and all fields are periodic in the east–west direction. The sea surface temperature (SST) distribution, which is held fixed in time in these simulations, consists of a general meridional gradient which is slightly larger near the center of the domain than at the northern and southern boundaries. The SST is invariant in the zonal direction. The domain size used for these simulations was 4100 km in meridional extent by 3000 km in the zonal dimension.

The choices of initial conditions, domain size, and horizontal resolution were based on a balance between a desire to resolve the phenomena under study and acceptable running time and memory allocation. The jet speed and perturbation amplitude were chosen so as to give a convenient baroclinic wave growth rate. The distribution of the 21 vertical levels was chosen so as to give high vertical resolution near the surface and near the tropopause; high vertical resolution in the boundary layer is crucial in this study and failure to adequately resolve the tropopause can lead to numerical difficulties.

The initialization procedure involves first specifying the jet profile at each level. Then, using the velocity field at the lowest level, a modified form of the balance equation is applied at the surface to obtain surface pressure. Using the surface pressure and wind field, the balance equation is applied at each level to obtain the geopotential field. Finally, an altitude independent, sinusoidal perturbation is added to the geopotential field and the geostrophic perturbation v component is determined.

Given such a baroclinically unstable initial state, rapid cyclogenesis may be anticipated. By 120 h, the minimum surface pressure falls to 965 mb in the adiabatic and inviscid simulation and to 984 mb with the second-order closure physics.

4. Results

4.1. Adiabatic and inviscid case

The results of the adiabatic and inviscid (AI) simulation in the present study are not entirely consistent with the SK model. While the frontal fracture, WEWF, and seclusion are present, there are also strong indications that an occlusion forms.

Frontal fracture is apparent at hour 72 in that the baroclinic zones associated with the warm and cold fronts are separated near the center of the incipient cyclone. The WEWF undergoes strong frontogenesis from hour 72 to hour 84. Fig. 1a shows the near surface potential temperature at hour 84. The frontal fracture and strong WEWF are apparent. A north–south cross section of potential temperature over the central 2/3 of the domain and from the surface to 500 mb at hour 84 is shown in Fig. 1b (the plane of the cross section is indicated in Fig. 1a). Note the extremely strong baroclinic zone delineating the WEWF near the north end of the cross section. The baroclinic zone to the south is the cold front. The plane of this cross section, which is normal to the WEWF, intersects the cold front at an oblique angle; the cold front is stronger than it appears in Fig. 1b. Fig. 1b also shows the early stages of the seclusion (note the relatively warm area in the center of the cross section). The results show that the WEWF weakens slightly from hour 84 to hour 120. The cross section of potential temperature for hour 120 shows the mature seclusion with the characteristic outward sloping baroclinic ring (Fig. 1c). This figure is quite similar to Fig. 10.19 of SK and Fig. 22 of Neiman et al. (1993), which show seclusions observed during the Alaskan Storms

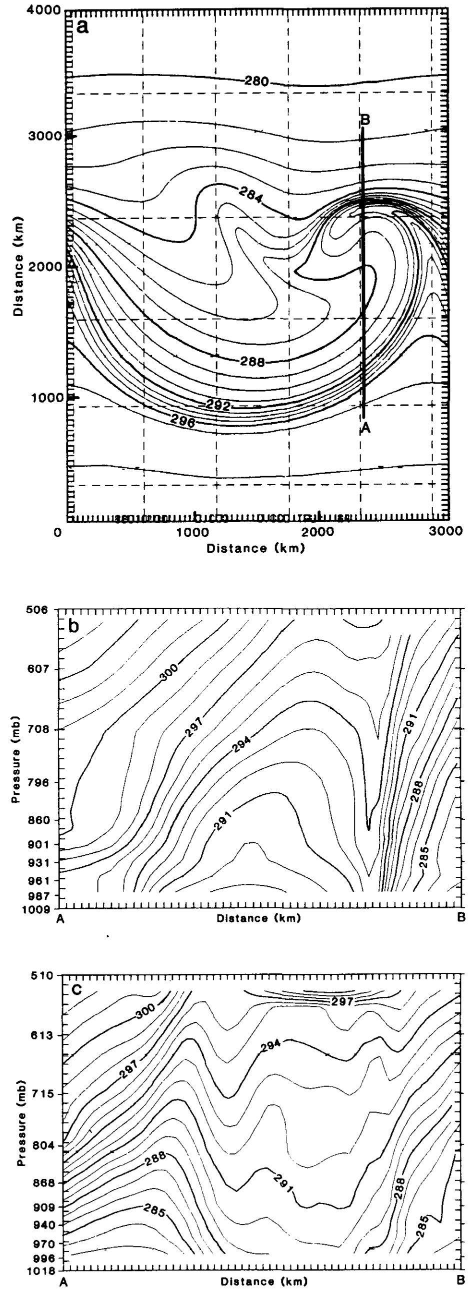

Fig. 1. (a) Near-surface potential temperature (K) at hour 84. (b) North–south cross section of potential temperature (K) for hour 84 (the plane of the cross section is shown in part (a). (c) North–south cross section of potential temperature (K) for hour 120. Contour interval: 1°K. (adiabatic and inviscid simulation)

Program on 10 March 1987 and during ERICA on 5 January 1989, respectively. The outward sloping baroclinic ring is clearly shown in both of these figures. The scale of the seclusion shown in Fig. 1c is comparable to the one shown in Fig. 10.19 of SK but considerably larger than the one shown in Fig. 22 of Neiman et al.

Terms of the frontogenetic forcing were evaluated in the vicinity of all of the fronts at 12 h intervals. This technique is discussed by Miller (1948) and Bluestein (1986). Frontogenetic forcing at the WEWF is due primarily to tilting and stretching deformation. Both tilting and stretching are dependent upon convergence. Integrated mass convergence gives rise to vertical motion and the stretching deformation is directly related to convergence. Weakening of the WEWF from hour 84 to 120 results primarily from decreasing convergence at the front. As convergence weakens, ascending motion (and, consequently, tilting frontogenesis) and stretching deformation weaken as well.

Close examination of the results suggests that the seclusion forms in the early stages of cyclogenesis between hour 72 and hour 96 (days 3 and 4) as relatively warm ambient air is "secluded" from the polar air stream as the warm front "wraps around" the low. The near surface potential temperature is above 290 K at hour 84 in the center of the low. Near hour 96, the frontal fracture appears to "heal" and the warm and cold fronts re-unite in the southeast quadrant of the low. At this point, the warm air begins to move aloft in the manner of the classical occlusion process. The near surface potential temperature distribution for 108 h (Fig. 2) is quite suggestive of these processes. The results indicate that the potential temperature in the center of the low never exceeds 290 K and the area enclosed by the 290 K isentrope grows smaller with time as the occlusion grows larger.

Evidence for the existence of an occlusion can be seen in cross sections of potential temperature from three planes at different latitudes for hour 108 (the planes of the cross sections are shown in Fig. 2). The warm air is seen to rise to the north from one plane to another. The warm air can be delineated by the location of the 288 K isentrope. In the southernmost cross section (Fig. 3a), the 288 K isentrope intersects the surface at two locations 400 km apart. In the intermediate cross section 400 km to the north (Fig. 3b), the intersections with the surface are 200 km apart and, in the northernmost cross section 400 km further north (Fig. 3c), there is only one intersection.

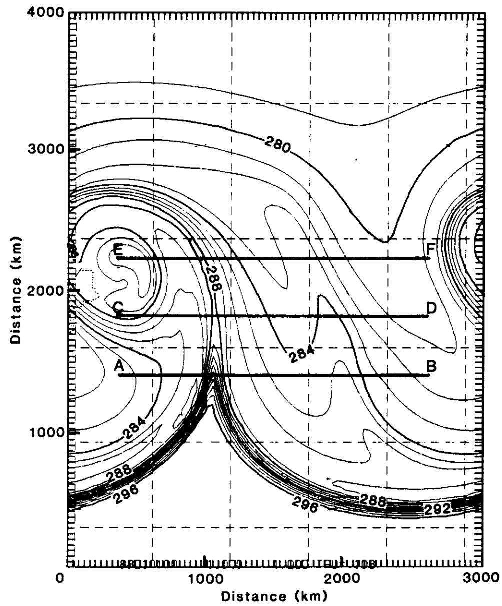

Fig. 2. Near-surface potential temperature field (K) at 108 h. Contour interval: 1°K. (adiabatic and inviscid simulation)

Published work by Shapiro and his co-workers subsequent to SK (Neiman and Shapiro, 1993; Keyser, 1993, personal communication) have alluded to the possibility of occlusions at various stages of cyclogenesis. This suggests that the model as presented by SK has perhaps been amended to some extent to include the possibility of an occlusion in later stages. In fact, Shapiro and Grell (1994) discuss the presence of a previously-unsuspected occlusion to the south of the WEWF (which they refer to as a "T-clusion") discovered in a re-analysis of the ERICA storm of 5 January 1989. The original analysis of this storm by Shapiro and his co-workers is described by Neiman et al. (1993).

The results of the AI simulation are generally consistent with the statement in SK that the adiabatic components of the flow are responsible for creating the essential features of cyclogenesis (i.e., the frontal fracture, seclusion and WEWF).

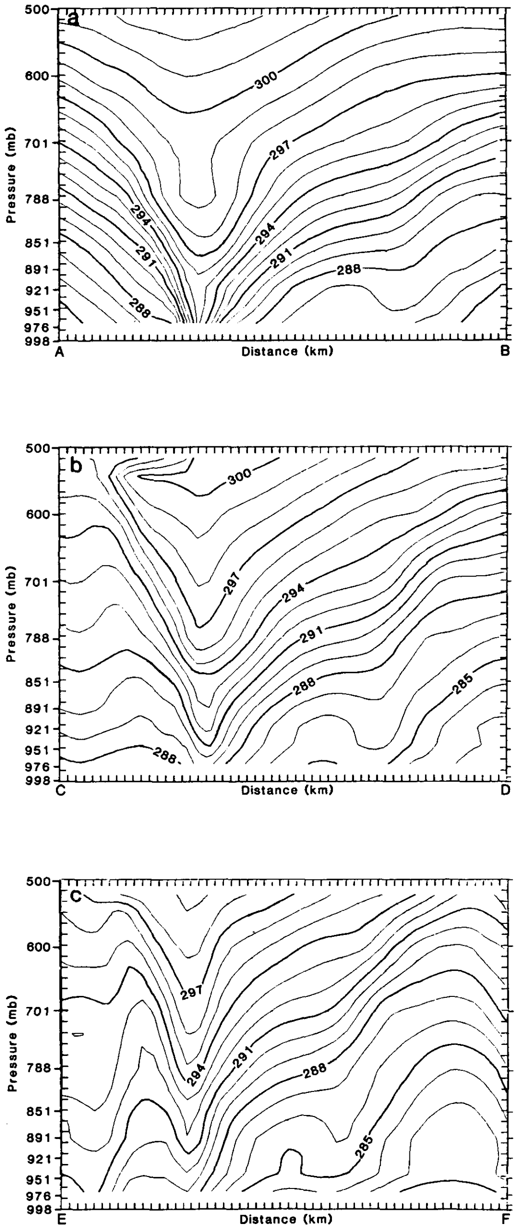

Fig. 3. (a) East–west cross section of potential temperature (K) for hour 108 (the plane of the cross section is denoted as AB in Fig. 2). (b) East–west cross section of potential temperature for hour 108 (the plane of the cross section is denoted as CD in Fig. 2). (c) East–west cross section of potential temperature for hour 108 (the plane of the cross section is denoted as EF in Fig. 2). Contour interval: 1°K. (adiabatic and inviscid simulation)

4.2. 2nd-order closure simulation

The results of the second-order closure simulation show that the inclusion of boundary layer physics has a profound effect on the simulation. While the warm front, cold front, WEWF, and seclusion are clearly present, they are much weaker in the present simulation.

The near-surface potential temperature distribution at hour 84 is shown in Fig. 4a. Comparison to the near-surface potential temperature at hour 84 for the AI case (Fig. 1a) shows that the baroclinic wave amplitude is smaller in this case and the potential temperature gradients associated with the warm and cold fronts are dramatically different from the AI case. There are several reasons for this. The wind speed is lower due to surface drag. Temperature gradients and, therefore, available potential energy are reduced due to upward surface heat flux in the cold air. Frontogenesis is reduced since the geostrophic horizontal deformation is weaker. Branscome et al. (1989) investigated the effect of surface heat and momentum fluxes on the nonlinear development of baroclinic waves. They found that nonlinear surface drag was most important in reducing wave amplitude relative to the inviscid case. This resulted from enhanced dissipation. Reduced wind speeds were also responsible for most of the reduction in horizontal heat transport at low levels.

A cross section of potential temperature at hour 84 (Fig. 4b) shows the WEWF and cold front to the south (the plane of the cross section is shown in Fig. 4a). As in Fig. 1b, the cold front at this time is actually stronger than it appears to be as the plane of the cross section intersects the cold front at an oblique angle. In contrast to the AI case, the WEWF does not weaken near the surface with time after hour 84. It does, however, strengthen considerably above 850 mb between hours 84 and 120. This is apparent in comparing the cross section of potential temperature for hour 108 (Fig. 4c) with that for hour 84 (Fig. 4b).

Frontogenetic forcing in this case is due primarily to tilting and stretching deformation, as in the AI case. The lack of frontolysis near the surface results from near surface convergence changing little with time from hours 84 to 120. While the maximum frontogenetic forcing in the AI case occurred near 850 mb, tilting frontogenesis in the present case extends well above 850 mb. This

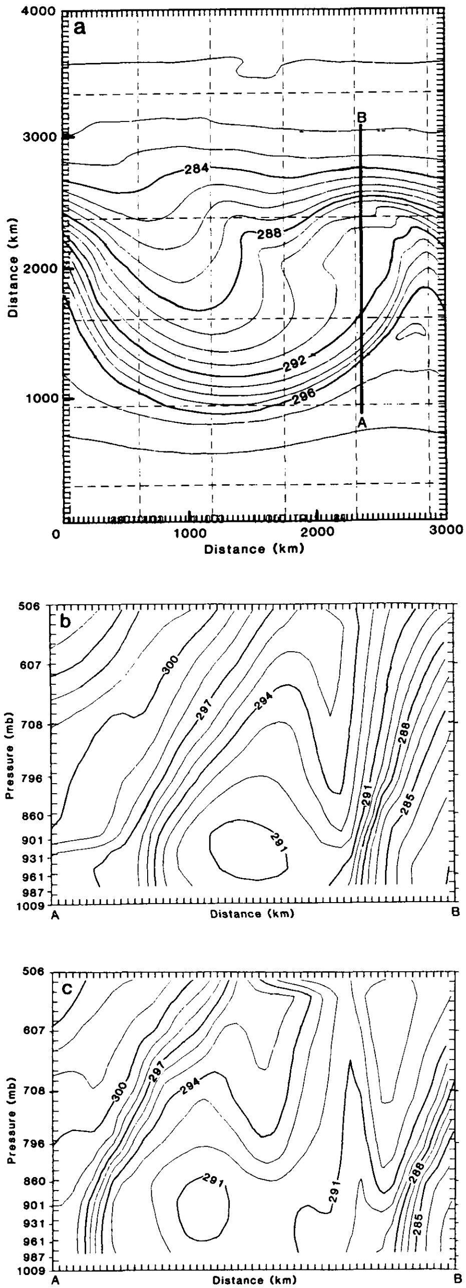

Fig. 4. (a) Near-surface potential temperature distribution (K) for hour 84. (b) North–south cross section of potential temperature (K) for hour 84 (the plane of the cross section is shown in part (a). (c) North–south cross section of potential temperature for hour 108. Contour interval: 1°K. (second-order closure simulation)

is consistent with the strengthening of the front at and above this level.

In this case, the seclusion is not as well-defined as in the AI case and does not extend to the surface. The southern side of the outward sloping baroclinic ring is not well-defined at hour 108, although there is a weak baroclinic zone extending from approximately 850 mb to 600 mb. At hour 84, the seclusion is most apparent at 850 mb. From hour 84 to hour 108, the seclusion extends upward and is most well-defined at 700 mb by hour 108 (see Fig. 5). This is entirely consistent with the results of Neiman and Shapiro (1993). In their investigation of a cyclogenesis event during ERICA, Neiman and Shapiro found the first evidence of a seclusion at 850 mb. The WEWF and seclusion then developed upward, reaching 500 mb after 18–24 h. The relatively small scale of the seclusion is also consistent with Neiman and Shapiro.

Strong evidence for the existence of an occlusion in this case is provided by examination of cross sections at different latitudes just as in the AI case. In southernmost cross section, selected isentropes delineating the warm air are seen to intersect the surface at locations a few hundreds of km apart.

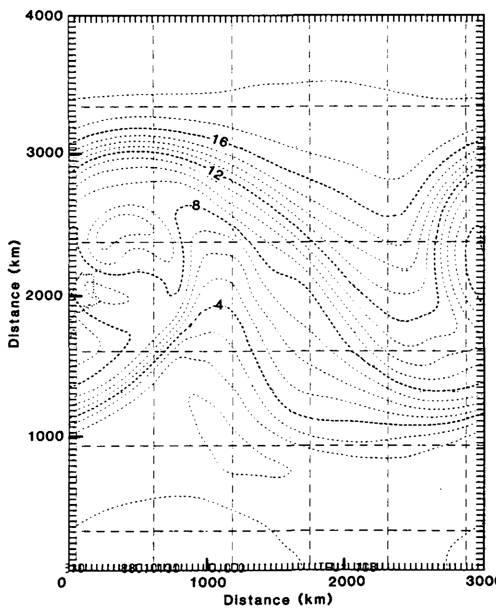

Fig. 5. 700 mb temperature field (C) at 108 h. Contour interval: 1°C. (2nd-order closure simulation)

At an intermediate location the intersections are closer together, and, in the northernmost cross section, the isentropes do not intersect the surface at all.

4.3. *Sensitivity studies*

Several sensitivity studies were conducted in an effort to further understand the impact of physical processes on the bent-back warm front and seclu-

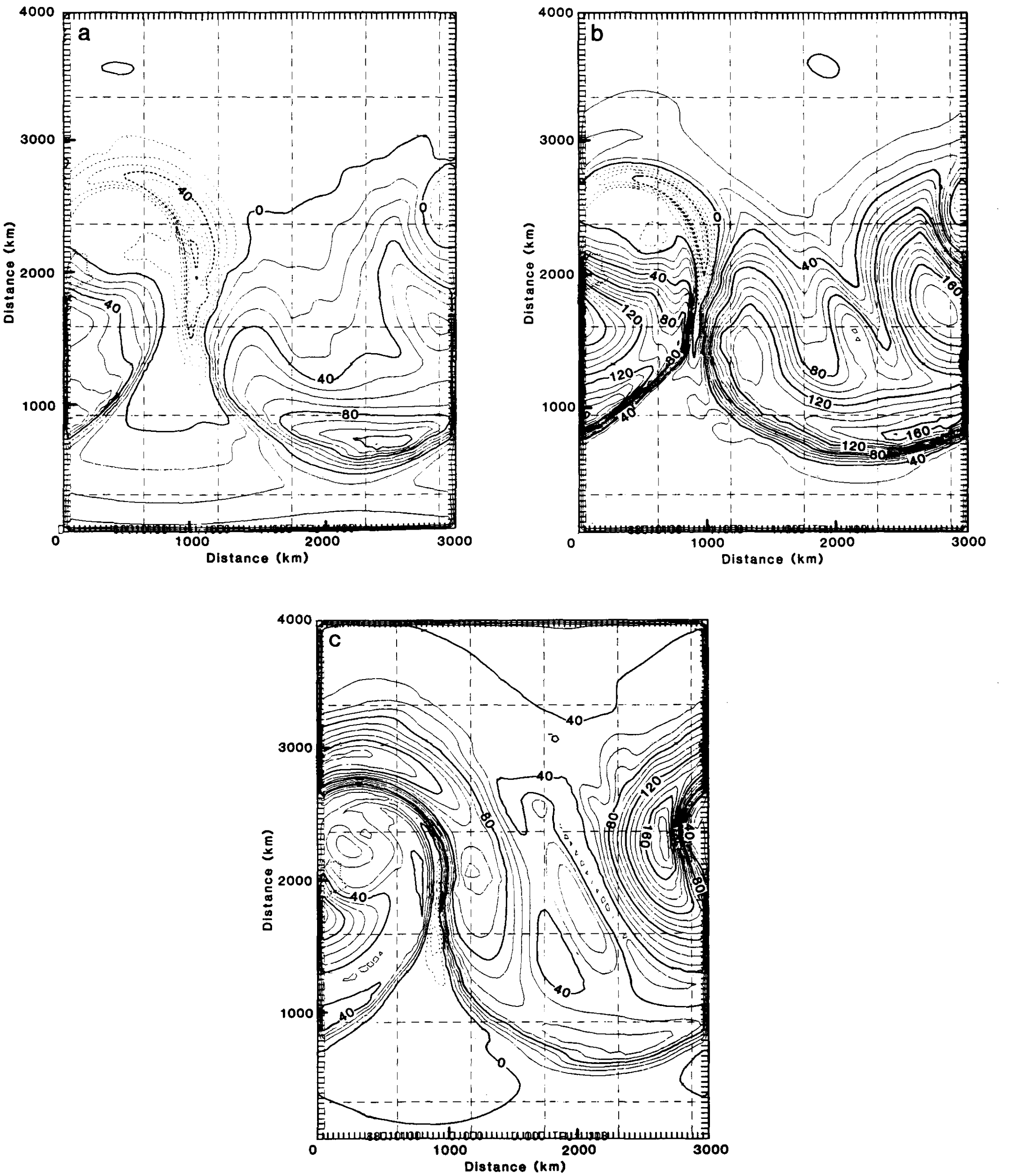

Fig. 6. Surface sensible heat flux distributions (W m^{-2}) at 108 h for the (a) 30°C gradient simulation, (b) original simulation, and (c) 10°C gradient simulation. Contour interval: 10 W m^{-2}.

sion. One of the sensitivity issues examined was the impact of surface sensible heat flux. In the simulations discussed above, the sea-surface temperature (SST) distribution consisted of a decrease of 20°C over 4000 km from the south boundary of the domain to the north boundary. The meridional gradient in SST was slightly larger near the center of the domain than it was near the boundaries. A simulation in which a constant meridional gradient in SST with the same 20°C change was used produced results very similar to those described above. Simulations were also performed using uniform gradients of 10°C and 30°C over 4000 km. In each case, the temperature near the center of the domain is the same. Thus, in simulations with larger gradients, the SST is warmer near the southern boundary of the domain and colder near the northern boundary. In the 10°C gradient simulation, the SST near the northern boundary is 286°K while, in the 30° gradient simulation, the SST at the same location is 271°K.

Shown in Fig. 6a is the surface sensible heat flux distribution (in W m^{-2}) for the 30°C gradient simulation at 108 h. Note the large region of downward heat flux in the vicinity of the bent-back warm front; the region of downward heat flux in excess of 60 W m^{-2} extends for over 1000 km. In

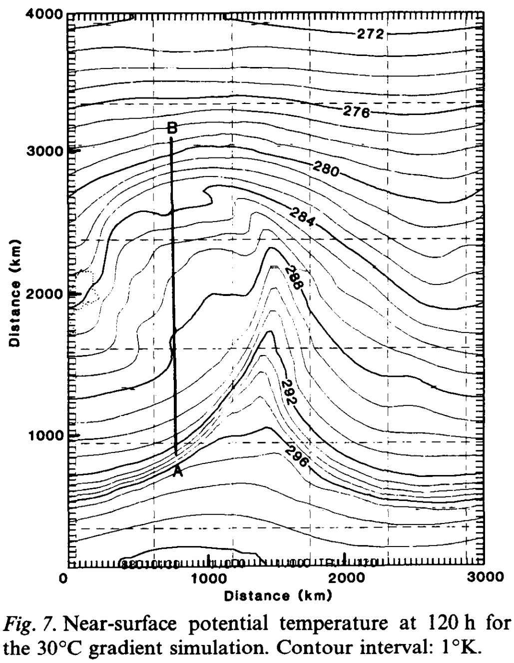

Fig. 7. Near-surface potential temperature at 120 h for the 30°C gradient simulation. Contour interval: 1°K.

the original simulation, the downward surface heat flux at 108 h extends along the bent-back warm front with values of 60 W m^{-2} occupying a region 400 km in extent (Fig. 6b). In the 10°C gradient simulation, there is no downward heat flux near the seclusion or bent-back warm front (there is a small "tongue" of downward heat flux along the occlusion) (Fig. 6c).

Turning now to the near-surface potential temperature distributions at 120 hours, the bent-back warm front and seclusion are difficult to identify near the surface in the 30°C gradient simulation (Fig. 7).The cross section of potential temperature at 120 h shows stable stratification from the cold front to the south to the bent-back warm front (Fig. 8). In the original simulation, the bent-back warm front is well defined on the north side of the occlusion and extends to the west side as well (Fig. 9). The cross section of potential temperature at 120 h shows a strong bent-back warm front with some evidence of the outward sloping baroclinic zones extending no lower than ~800 mb in the vicinity of the seclusion (Fig. 10). In the 10°C gradient simulation at 120 h, the bent-back warm front is quite strong and extends nearly all the way around to the south side (Fig. 11). The cross section of potential temperature from this simulation at 120 h clearly shows the strong bent-back warm front and outward sloping baroclinic ring characteristic of the seclusion (Fig. 12). The seclusion extends all the way to the surface in this case.

The results of the sensitivity study indicate that surface sensible heat flux exerts a large influence on the structure of the seclusion and the WEWF. In

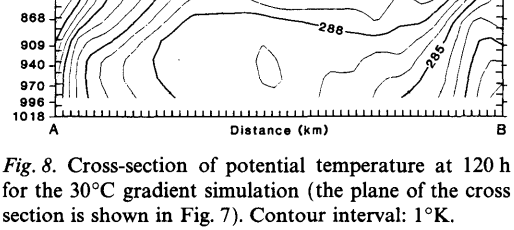

Fig. 8. Cross-section of potential temperature at 120 h for the 30°C gradient simulation (the plane of the cross section is shown in Fig. 7). Contour interval: 1°K.

Tellus A/47/5:1-15

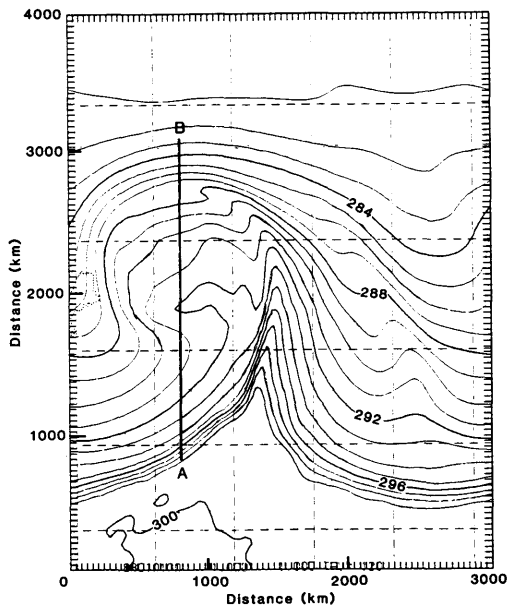

Fig. 9. Near-surface potential temperature at 120 h for the original simulation. Contour interval: 1°K.

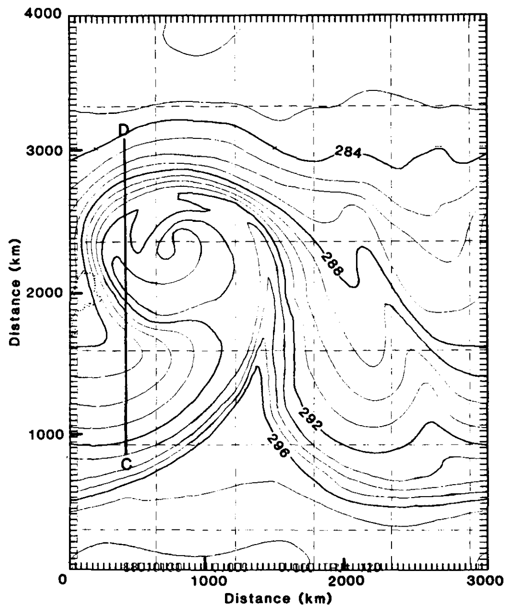

Fig. 11. Near-surface potential temperature at 120 h for the 10°C gradient simulation. Contour interval: 1°K.

the presence of large downward heat flux, as in the 30°C gradient simulation, the seclusion does not form. When the heat flux is upward, as in the 10°C gradient simulation, the seclusion is well-defined and extends to the surface. In the intermediate case, the seclusion is not identifiable below 850 mb due to cooling at low levels resulting from downward heat flux. The WEWF is present in all three cases. It is strongest in the intermediate case and extremely weak in the 30°C gradient case. This is the result of cooling on the north (warm) side of the front in the 30°C gradient case and warming on the south (cold) side of the front in the 10°C gradient case. In both of these cases, surface heat flux exerts a strong frontolytic effect on the WEWF.

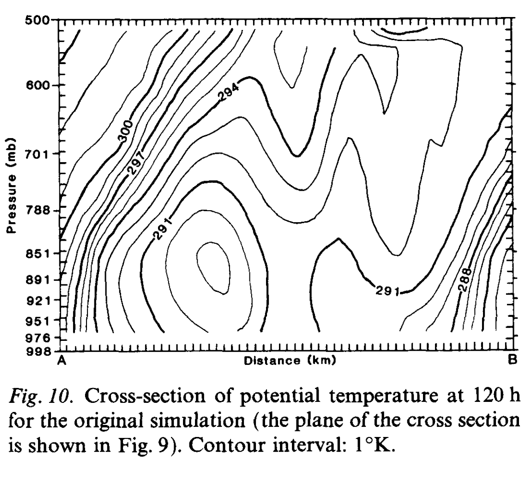

Fig. 10. Cross-section of potential temperature at 120 h for the original simulation (the plane of the cross section is shown in Fig. 9). Contour interval: 1°K.

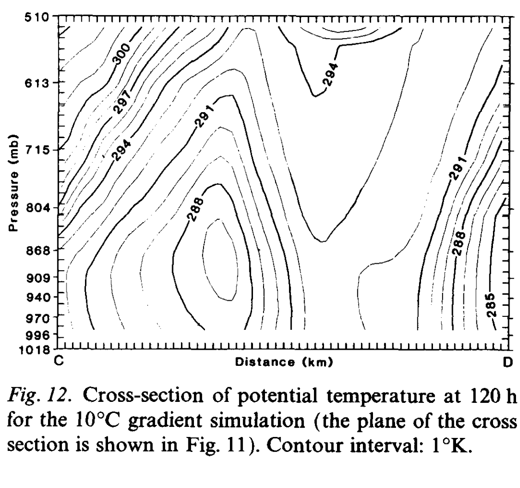

Fig. 12. Cross-section of potential temperature at 120 h for the 10°C gradient simulation (the plane of the cross section is shown in Fig. 11). Contour interval: 1°K.

5. Discussion

The results of the 2nd-order closure simulation differ from those for the AI, although the frontal fracture, WEWF, seclusion, and occlusion are all present. In summary, the primary differences between the AI and second-order closure simulations are as follows: (1) The WEWF (and other fronts) are weaker in the second order closure simulation; (2) above 850 mb, the WEWF strengthens from hour 84 to hour 120 in the second-order closure simulation; (3) near the surface, the strength of the WEWF changes little with time in the second-order closure simulation while the WEWF weakens with time in the AI simulation; (4) the seclusion is less well-defined and does not extend below 850 mb in the second-order closure simulation.

These differences result from the action of parameterized boundary layer physics. The weakness of frontal features results from surface sensible heat flux cooling the warm air and from a reduction in the frontogenetic effects of both shearing and stretching deformation due to a reduction in wind speed resulting from surface stress. Strengthening of the front above 850 mb results from tilting frontogenesis in the second-order closure simulation. Near the surface, the differences in frontal strength are due to differences in the convergence. In both simulations, an imbalance between the wind and mass fields results in an increase in divergence (decreasing convergence) as proposed by Orlanski et al. (1985). In the second-order closure simulation, this is offset by convergence due to frictional turning of the wind toward low pressure. In the adiabatic and inviscid simulation, no such mechanism exists and the convergence decreases with time. The weakness in the seclusion below 850 mb results from downward surface heat flux. When downward heat flux is reduced due to warmer SST, the seclusion and WEWF are well-defined and extend to the surface.

The results of the sensitivity studies are complemented by the work of Kuo and Low-Nam (1994), in which a sensitivity study on surface friction is presented. In simulations of the *Ocean Ranger* storm, the diabatic effect of surface fluxes was removed and three different specifications of surface roughness were used. Their results showed that, when surface roughness typical of continental surfaces was used (LAND), no seclusion formed. The WEWF was also much weaker in the LAND case. In simulations with oceanic surface roughness and no surface friction, the warm core seclusion was present and similar to full physics simulations performed by Kuo et al. (1992). These results are consistent with those of Hines and Mechoso (1993), in which differing (constant) values of the drag coefficient were used in simulations of cyclogenesis. The use of relatively large drag coefficients representative of continental surfaces resulted in the disappearance of the WEWF.

Thus, the present results taken in combination with those of Kuo and Low-Nam (1994) and Hines and Mechoso (1993) show that large downward surface fluxes of heat and momentum inhibit the formation of the seclusion and WEWF.

6. Conclusions

In conclusion, the results suggest that introduction of concepts of the frontal fracture and WEWF in the SK model constitute an important contribution to the understanding of the life cycle of baroclinic waves and fronts. The shortcoming of the model is that it fails to account for the last stage of the life cycle in which the model shows the warm and cold fronts reuniting, leading to the development of an occlusion. Subsequent refinements to the model include the introduction of the occlusion to the south of the WEWF. While the adiabatic components of the motion create the structural features of the model, boundary layer physical processes determine the strength and horizontal extent of the bent-back warm front and seclusion.

While it is hardly surprising that surface physical processes play an important role in cyclogenesis, the precise impact of these processes in the context of the SK model is a topic deserving of further investigation. The incorporation of the occlusion in the SK model as discussed by Shapiro and Grell (1994) suggests that the model is evolving and maturing with time as it gains acceptance in the scientific community. The inclusion of the effects of surface physical processes into the existing framework will constitute a major advance.

7. Acknowledgments

The support of the sponsor, Office of Naval Research, Program Element 0601153N, is acknowledged. The author benefited from discussions of this work with Dr. S. Burk, head of the Local Scale Simulation Section of the Marine Meteorology Division of the Naval Research Laboratory and Dr. James Doyle and Dr. Chi-Sann E. Liou of the Mesoscale Modeling Section. The assistance of Mr. S. Bishop, head of the Technical Publications Section, in preparing the figures is gratefully acknowledged.

REFERENCES

Bluestein, H. B. 1986. Fronts and jet streaks: a theoretical perspective. In: *Mesoscale meteorology and forecasting*, P. S. Ray, ed. American Meteorological Society, Boston, MA. 793 pp.

Branscome, L. E., Gutowski, J. and Stewart, D. A. 1989. Effect of surface fluxes on the nonlinear development of baroclinic waves. *J. Atmos. Sci.* **46**, 460–470.

Burk, S. D. and Thompson, W. T. 1989. A vertically-nested regional numerical weather prediction model with second-order closure physics. *Mon. Wea. Rev.* **117**, 2305–2324.

Hines, K. M. and Mechoso, C. 1993. Influence of surface drag on the evolution of fronts. *Mon. Wea. Revv.* **121**, 1152–1175.

Hodur, R. M. 1987. Evaluation of a regional model with an update cycle. *Mon. Wea. Rev.* **115**, 2707–2718.

Kuo, Y.-H. and Low-Nam, S. 1994. Effects of surface friction on the thermal structure of an extratropical cyclone. Preprints, *International Symposium on the life cycles of extratropical cyclones*, 27 June–1 July, 1994, Bergen, Norway.

Kuo, Y.-H., Reed, R. J. and Low-Nam, S. 1992. Thermal structure and airflow in a model simulation of an occluded marine cyclone. *Mon. Wea. Rev.* **120**, 2280–2297.

Liu, T., Katsaros, K. and Businger, J. 1979. Bulk parameterization of air-sea exchanges of heat and water vapor including the molecular constraints at the interface. *J. Atmos. Sci.* **36**, 1722–1735.

Mellor, G. L. and Yamada, T. 1974. A hierarchy of turbulence closure models for planetary boundary layers. *J. Atmos. Sci.* **31**, 1791–1806.

Miller, J. E. 1948. On the concept of frontogenesis. *J. Meteor.* **5**, 169–171.

Neiman, P. J. and Shapiro, M. A. 1993. The life cycle of an extratropical marine cyclone. Part I: Frontal-cyclone evolution and thermodynamic air-sea interaction. *Mon. Wea. Rev.* **121**, 2153–2176.

Neiman, P. J., Shapiro, M. A. and Fedor, L. S. 1993. The life cycle of an extratropical marine cyclone. Part II: Mesoscale structure and diagnostics. *Mon. Wea. Rev.* **121**, 2177–2199.

Orlanski, I., Ross, B., Polinsky, L. and Shaginaw, R. 1985. Advances in the theory of atmospheric fronts. In: *Advances in geophysics*, vol. **28**: *Issues in atmospheric and oceanic modeling*, Part B: *Weather dynamics*. S. Manabe, ed. Academic Press, New York, NY. 432 pp.

Shapiro, M. A. and Grell, E. D. 1994. In search of synoptic/dynamic conceptualizations of the life cycles of fronts, jet streams, and the tropopause. Preprints, *International Symposium on the life cycles of extratropical cyclones*, 27 June–1 July, 1994, Bergen, Norway.

Shapiro, M. A. and Keyser, D. 1990. Fronts, jet streams, and the tropopause. In: *Extratropical cyclones. The Erik Palmén Memorial Volume*, C. Newton and E. O. Holopainen, eds. American Meteorological Society, Boston, MA. 262 pp.